RESEARCH PAPER

Welding characteristics and microstructure of an industrially processed Fe-Mn-Al-Ni shape memory alloy joined by tungsten inert gas welding

Vincent Fabian Viebranz[1] · Thomas Hassel[1] · Thomas Niendorf[2] · Hans Jürgen Maier[1]

Abstract

Iron-based shape memory alloys have recently attracted increased attention due to their low material costs combined with good workability and high transformation strains. They show excellent welding properties, as shown by several studies and compared to non-iron-based shape memory alloys, and are potential candidate materials for large-scale application as damping elements in building structures. Since subsequent heat treatment is only possible to a limited extent for large-scale components, it is necessary to minimize the effects of processing and welding operations on the shape memory properties. Therefore, a suitable microstructure must be established in the heat-affected zone and the fusion zone during the welding process. Thus, industrially processed polycrystalline Fe-Mn-Al-Ni was joined by tungsten inert gas welding with matching filler material. The phases formed upon welding with different parameters were investigated using optical microscopy, scanning electron microscopy and X-ray diffraction. Shielding gas composition as well as mean arc linear energy have a huge impact on the γ-phase precipitation. Intercrystalline cracking can be supressed by increasing the γ content. Further, the α-fraction and grain size in the fusion zone can be controlled by the welding parameters. Ultimately, a hardness value of the fusion zone equal to heat-treated material was achieved which suggests that the fusion zone may be able to transfer the stress required for martensitic transformation.

Keywords Iron-based shape memory alloy · Tungsten inert gas welding · Fe-Mn-Al-Ni · Process parameters · α/γ-phase ratio · Pre-weld heat-treatment

1 Introduction

Due to low alloying cost and good processability, iron-based shape memory alloys (SMA) have attracted substantial interest in recent decades [1–5]. Promising Fe-based alloy systems are Fe-Ni-Co-Al-X (X = Ta, Nb, Ti) [6–8] and Fe-Mn-Al-Ni-X (X = Ti, Cr) [1, 9, 10]. The Fe-Mn-Al-Ni system features a unique phase transformation, which is related to a change of the α/γ equilibrium. The altered α/γ equilibrium results in a γ-solvus temperature of near 1430 K and a stabilisation of the γ-phase at room temperature [1, 11]. In conventional Fe-based systems, a martensitic transformation (MT) of an austenitic γ-fcc phase to a martensitic α'-bcc or bct phase and in some cases to an ε-hcp phase can be observed. $FeMn_{34}Al_{15}Ni_{7.5}$ (at.%), however, undergoes a MT of a parent α-bcc high-temperature phase, also referred to as austenite in this system, to a martensitic γ'-fcc product phase [1]. In particular, it is characterised by a low slope of the Clausius-Clapeyron relation of 0.53 MPa K^{-1}, whereas for the widely used NiTi alloys, $d\sigma_c/dT$ typically varies between 5 and 8 MPa K^{-1}. This clearly demonstrates a minor temperature dependence of the stress-induced MT. Thus, the shape memory effect can be exploited even at room temperature in single crystalline and polycrystalline materials [12–14].

Polycrystalline Fe-SMAs typically suffer from rapid degradation of their functionality upon cyclic loading, as both the elastic properties and the MT are anisotropic [14, 15]. In addition, only a few martensite variants form in Fe-SMAs [16]. This leads to high stresses between grains with different orientations and, eventually, to structural failure

✉ Vincent Fabian Viebranz
viebranz@iw.uni-hannover.de

1   Institut Für Werkstoffkunde (Materials Science), Leibniz Universität Hannover, 30823 Garbsen, Germany

2   Institut Für Werkstofftechnik (Materials Engineering), Universität Kassel, 34125 Kassel, Germany

nucleating at grain boundaries at high loads. Especially triple junction grain boundaries cause fast functional degradation, as the stress concentration activates unfavourably interacting martensite variants [17–19]. Thus, by increasing the grain size, pseudoelasticity can be significantly improved. Through Abnormal Grain Growth (AGG), Omori et al. were able to induce so-called bamboo-like microstructures with a ratio of grain diameter d to wire diameter D or a grain diameter to sheet thickness t ratio of greater than one [1, 11, 20, 21]. In addition, failure along grain boundaries can be further delayed by controlled cooling conditions. Specifically, the ductile γ-phase can be precipitated along the grain boundaries, which curtails intergranular crack formation [22].

The low cost, good processability and high reversibility makes Fe-based SMAs suitable for application in damping elements in building structures [23, 24]. Therefore, several studies have already been devoted to the welding behaviour of Fe-SMAs. Various studies addressed laser welding and tungsten inert gas (TIG) welding of Fe-Mn-Si [25, 26], as well as electron beam welding and induction butt welding of Fe-Mn-Al-Ni [27, 28]. During induction butt welding of, the evolution of a large α-fraction in the fusion zone (FZ) is seen, while the γ-phase forms only along the grain boundaries and is more prominent in the heat affected zone (HAZ). When using an AGG heat treatment, a bamboo-like structure can be established despite the weld structure. However, the grain boundaries of the newly formed and abnormally grown α-grains partially run along the previous HAZ [28]. So far, no study investigated the welding behaviour and microstructure of Fe-SMAs joined using matching filler material, and the present study was designed to address this issue.

A particular challenge for actual components is often the heat treatment of the welded material. If the components are characterized by very large dimensions, heat treatment after welding might not be possible. In order to maintain the shape memory properties, a microstructure with high α-phase content must already be established in the HAZ and the FZ during the welding process. In the present study, industrially processed polycrystalline Fe-Mn-Al-Ni sheets were joined and the welding behaviour was correlated with the microstructural evolution. The latter was characterized using optical microscopy (OM), scanning electron microscopy (SEM) and X-ray diffraction (XRD). TIG was chosen, as this is a widely used welding process conventionally employed for the applications in mind. Bead on plate welds and square butt welds with matching filler material (cf. Section 2) were carried out to understand the effect of the mean arc linear energy onto the formed phases. By varying the process parameters, a weld structure should be achieved that does not suffer from a rapid loss of functional properties even without subsequent heat treatment.

2 Experimental

2.1 Material and processing

Fe-Mn-Al-Ni ingots with a nominal composition of $FeMn_{34}Al_{15}Ni_{7.5}$ (at.%) were produced by thyssenkrupp Steel Europe AG (Duisburg, Germany) using industrial process routes. After melting, the ingots were hot-rolled to a thickness of 2 mm. As initial material for the matching filler material, strips with a cross-section of 2 mm × 2 mm and a length of 1500 mm were cut from the same sheets by abrasive water jet cutting. In order to allow wire drawing without the need of intermediate annealing, a high γ content has to be present in the Fe-Mn-Al-Ni material. Thus, the strips were first solution annealed under Ar atmosphere at 1473 K for 5 min and then air-cooled down to room temperature (298 K). Subsequently, the strips were heat-treated a second time at 1073 K for 5 min and again air-cooled to finally obtain a high fraction of the ductile γ-phase. In order to remove any scaling layer that may have been formed, the heat-treated strips were first rubbed gently with steel wool and then cleaned with ethanol. After heat treatment, the strips were rounded by cold-rolling and finally cold-drawn to a wire diameter of 2 mm ($\varepsilon = 21.5\%$).

2.2 Welding

For the welding tests, specimens with a length of 80 mm and a width of 60 mm were machined using abrasive water jet cutting. Finally, the surfaces were cleaned by sandblasting and subsequent rinsing with ethanol to remove any residual contamination. The weld seams were aligned parallel to the rolling direction. First, bead on plate welds were carried out using the 2 mm thick sheet material without any filler material. For welding, an EWM TETRIX 521 AC/DC COMFORT FWD source was used in direct current mode with a current of 110 A and a welding speed of approx. 300 mm/min. To investigate the influence of shielding gas composition on the as-welded microstructure and arc stability, the gas composition was varied between an 80/20 Ar/He and a 70/30 Ar/He mixture. During the welds, a constant flow rate of 12 L/min was maintained. In addition, square butt welds of the sheet material with 70/30 Ar/He were carried out. In this case, the EWM source was used along with a MOTOMAN HP20 robot to ensure a constant welding speed. The welding parameters used for the square butt welds are shown in Table 1. Since the filler material was placed on top of the welds, the wire feed speed equalled the torch speed. In order to study the effects of the mean arc linear energy on microstructure, the welding speed was varied between 300 and 400 mm/min and the welding current between 120 and 160 A.

Table 1 Welding parameters used for obtaining square butt welds by TIG welding with matching filler material; voltage readout of the power supply at an arc length of 3 mm is given; the wire feed speed equalled the torch speed (cf. section Experimental)

Conditions					
Welding shape	Current (A)	Voltage (V)	Welding speed (mm/min)	Filler material	Shielding gas
Square butt weld	120, 130,140	16.7, 16.7,17	300	Matching (ø = 2 mm)	70/30 Ar/He
	140, 150, 160	20.3, 21.5, 23	400		

In order to investigate whether the initial grain morphology of the base metal has an influence on the phases in the HAZ and the FZ, a set of specimens was solution annealed at 1473 K for 15 min and then air-cooled prior to welding. The heat-treated specimens were cleaned and then welded with 105 A, also with welding speed of approx. 300 mm/min.

2.3 Characterization

After welding, cross-sections of the specimens were prepared for metallographic examination. The specimens were first ground and then polished (0.06 μm) using a VIBRO-MET 2. After polishing the cross-sections were etched with a solution of 2% HNO_3 (ROTH, 68%, pure) in ethanol (CVH, 99%). OM was performed on a ZEISS OLYMPUS BX53M. For SEM studies of the etched specimens a VISITEC MIRA XV was used at an accelerating voltage of 20 kV and a beam current of 70–150 pA. The SEM was equipped with a back-scattered electron (BSE) detector and a detector for energy dispersive X-ray spectroscopy (EDS). XRD was performed on a BRUKER D8 using Co-K_α radiation in an angular range

Table 2 Chemical composition of the 2 mm thick hot-rolled ingot measured by ICP-OES

Specimen	Composition (at.%)				
	Mn	Al	Ni	S	Fe
1	32	13.5	7.5	0.5	Balance
2	33.1	14.3	7.6	0.6	Balance
3	31.9	13.9	7.4	0.6	Balance
Average	32.3	13.9	7.5	0.6	Balance
Nominal	34	15	7.5	-	Balance
Literature [1]	34	15	7.5	0	43.5

from 45 to 120°2Θ with a spot size of 0.3 mm. Inductively coupled plasma optical emission spectroscopy (ICP-OES) using a SPECTRO CIROS VISION EOP was conducted to measure the composition of the base material (BM) and filler material prior to welding. Since both the BM and the filler material were cut from the same 2 mm thick hot-rolled ingot, three equivalent specimens where taken from the same ingot for ICP-OES. Vickers microhardness measurement ($HV_{0.3}$) of the as-welded state were carried out using a QNESS

Fig. 1 OM of polished and etched cross-sections of the bead on plate welds (a) 80/20 Ar/He and (b) 70/30 Ar/He (red arrow indicates EDS line scan); chemical composition along the BM, the HAZ and the FZ for a shielding gas composition of (a) 80/20 Ar/He and (b) 70/30 Ar/He; bead on plate welds (without filler material) with 110 A, welding speed of 300 mm/min and a constant flow rate of the shielding gas of 12 L/min
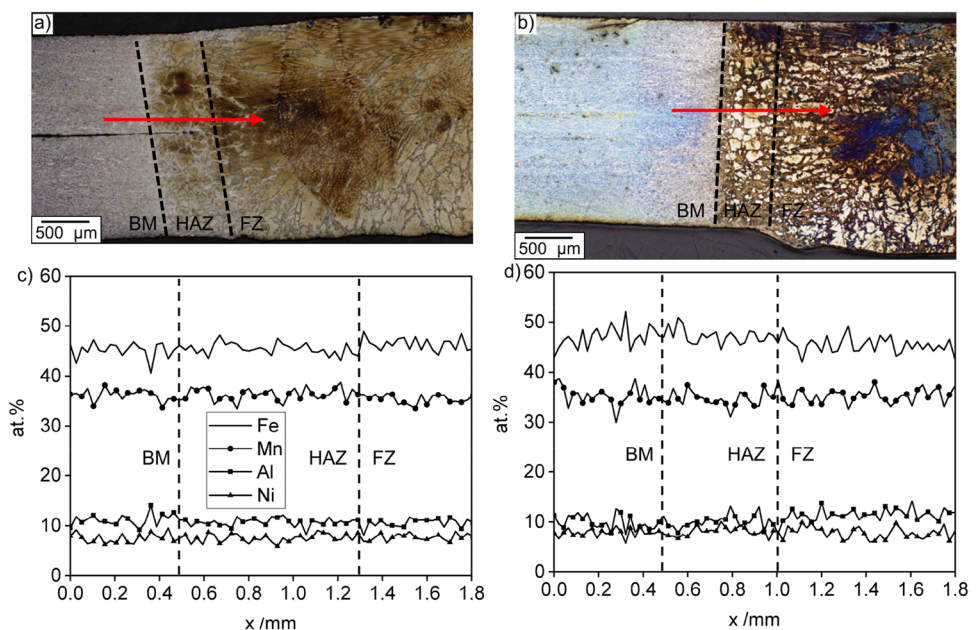
Q10 A + . The Hardness was measured in the middle of a cross-section with a distance of 1 mm to the surface.

3 Results and discussion

3.1 Bead on plate welds

The chemical compositions measured by ICP-OES are shown in Table 2. The average composition deviates from the nominal composition by 1–1.7 at.% for both the Mn-content and the Al-content.

In order to determine if a significant loss of alloying elements has occurred in the HAZ and the FZ during the welding process, the chemical composition of the HAZ and FZ of the bead on plate welds was determined by EDS line scans. Figure 1 shows OM images of the polished and etched cross-section of the bead on plate welds with a welding current of 110 A, a welding speed of approx. 300 mm/min and a shielding gas composition of 80/20 Ar/He (Fig. 1a) and a.

shielding gas composition of 70/30 Ar/He (Fig. 1b). In both images the position and length of the EDS line scan is shown (red arrow). When the EDS line scan data are taken into account (Fig. 1c and d), no significant differences in the chemical composition in the individual zones are present for both welding conditions. This demonstrates that the selective loss of alloying elements during the welding process is negligible. It has to be noted that EDS data typically have an absolute error of 2–5%. However, the technique is much more accurate when it comes to detecting relative changes. In the context of determining the selective loss of alloying elements, only the latter is important.

The OM images of the FZ of the bead on plate welds are shown in Fig. 2a and b. A comparison of the FZ shows that intergranular cracks occur on welds formed with a lower He content in the shielding gas. As shown in [29], the arc voltage and the anode temperature increase with increasing He content. This affects the temperature–time path upon cooling, which in turn leads to an altered γ-phase precipitation in the FZ. A low fraction of the ductile γ-phase along the grain boundaries results in high internal stresses and ultimately to an increased susceptibility to solid-state cracking. The comparison of Fig. 2a and b reveals that this effect can be exploited to enhance the γ-phase precipitation and suppress the intergranular cracking via adjusting the He content (toward higher contents) in the shielding gas. Furthermore, the higher heat input slows down the solidification rate and subsequent cooling and, thus, increases the size of the α-grains in the FZ.

Comparing SEM images of the FZs (Fig. 2c and d), a higher γ-phase fraction in Fig. 2d due to the higher heat input (and slower cooling) becomes apparent, while in

Fig. 2c the α-phase dominates. At the same time, γ' martensite needles (white lines) can also be identified within the α-phase in Fig. 2c. Residual stresses can be compensated by plastic deformation of the γ-phase regions before the stresses required to trigger the MT are reached in the grain interior. This effect is more pronounced the higher the γ-phase content is. Therefore less γ' martensite is evident in the FZ welded with 70/30 Ar/He.

In order to determine the γ-phase fractions in the FZ of the different bead on plate welds, the phases were characterized by XRD. Figure 2e and f shows the diffraction patterns of the FZs corresponding to the microscopic images in Fig. 2a-d. In the case of Fig. 2f (welded with 70/30 Ar/He), the relative intensity of the γ-phase is substantially higher than in Fig. 2e (welded with 80/20 Ar/He). In addition to the higher relative intensity of the
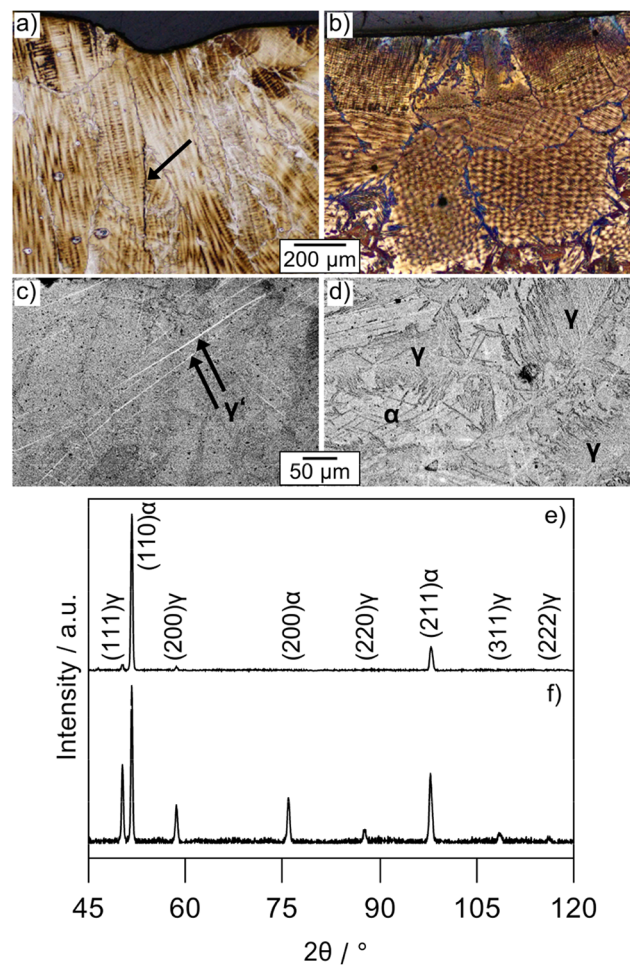

Fig. 2 OM of polished and etched cross-sections of the FZ of the bead on plate welds (110 A, 300 mm/min, 12 L/min) (a) 80/20 Ar/He (arrow indicates intergranular cracking) and (b) 70/30 Ar/He; SEM images at higher magnification of (a) and (b) are shown in (c) and (d), respectively; XRD patterns with subtracted background of the FZ for the bead on plate welds with (e) 80/20 Ar/He and (f) 70/30 Ar/He

γ-phase, the intensities of the individual α-phase diffraction peaks are also more intense in Fig. 2f than in Fig. 2e. This indicates a more random orientation of the α-grains, whereas Fig. 2e indicates a preferred orientation of the grains. The irregular orientation stems from an accumulation of small α-grains in the centre of the weld seam. The small α-grains formed when the solidification fronts met in the weld seam centre but have not grown during cooling nor were these dissolved by grain growth of the surrounding larger grains. As shown in Fig. 2c and d, pores and precipitates occur in the FZs.

Using EDS, the precipitates were identified as MnS and Al_2S_3. These precipitates are formed as sulphur is present in the alloy representing an impurity (Table 2). The effect of the pore formation and the change in effective matrix composition associated with the precipitates on the shape memory effect needs to be investigated in future studies. It should be noted that large α-grains, being more frequent upon welding using 70/30 Ar/He, are favourable with respect to pseudoelasticity.

3.2 Square butt welds

Based on these findings, the square butt welds were also created with a shielding gas composition of 70/30 Ar/He in order to obtain larger α-grains and a lower susceptibility to intergranular cracks. The square butt welds were joined using matching filler material. In order to be able to establish a low γ-phase fraction, the influence of the mean arc linear energy on the microstructure of the FZ was investigated. The mean arc linear energy can be determined by $Q = (U I \eta)/v$ $(\eta = 0.6)$ according to the standard DIN EN 1011–1, where U, I and v are arc voltage, current and welding speed, respectively.

Figure 3 shows cross-sections of the FZs of the square butt welds. A defect-free microstructure has been formed in all FZs. The large α-grains (dark) indicate an overall low solidification rate. The γ-phase (bright) has mainly formed along the grain boundaries. With increasing mean arc linear energy, the size of the α-grains increases (Fig. 3f). As observed during the bead on plate welds, the increased

Fig. 3 OM of the FZ of the square butt welds with matching filler material and 70/30 Ar/He; welding parameters are: (a) 120 A, v = 300 mm/min, (b) 130 A, v = 300 mm/min, (c) 140 A, v = 300 mm/min, (d) 140 A, v = 400 mm/min, (e) 150 A, v = 400 mm/min and (f) 160 A, v = 400 mm/min; calculated mean arc linear energy is given beneath each individual micrograph
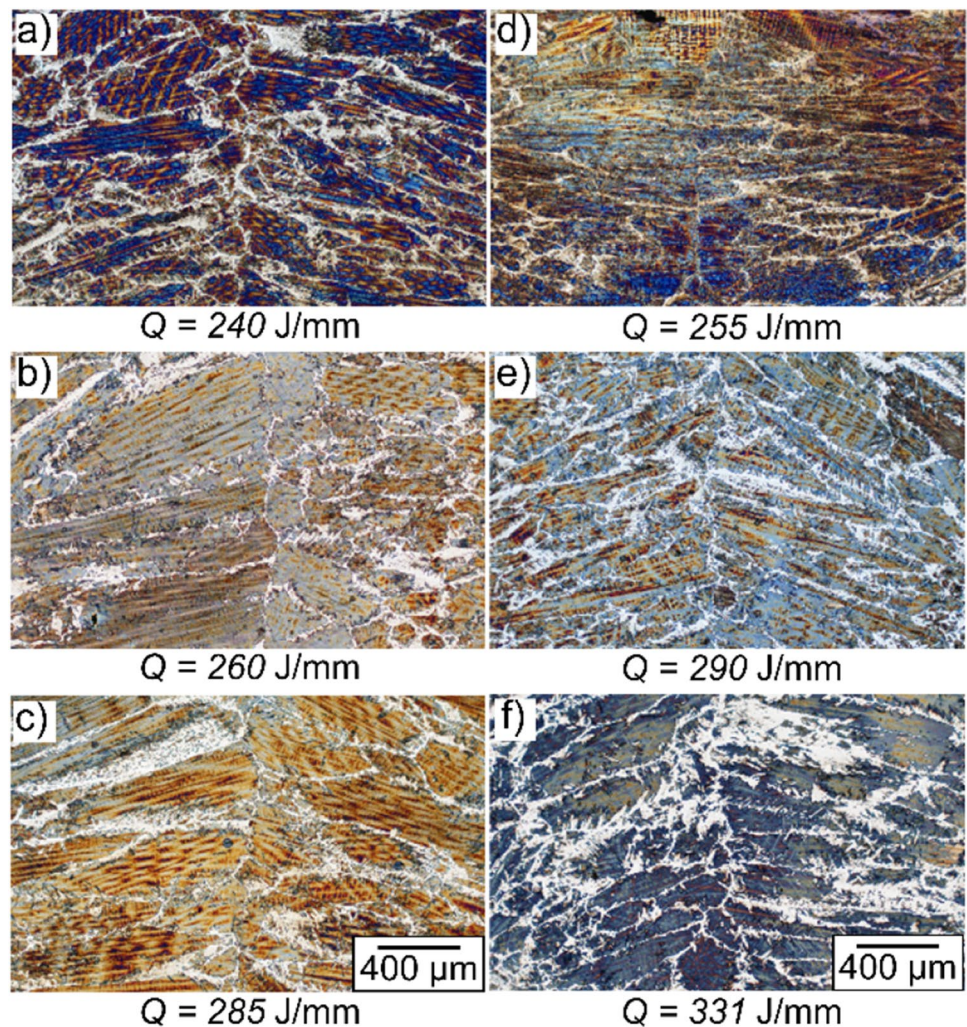
heat input leads to a lower cooling rate, thus enhancing the α-grain growth. While in Fig. 3a the average length of the α-grains of the major axis of the elongated grains is 510 μm, this increases to 720 μm in Fig. 3f. Besides the growth of the α-grains, a higher γ-phase fraction is present in Fig. 3f as compared to Fig. 3a.

When comparing the relative intensities of the phases in Fig. 4, it is noticeable that Fig. 4a and c indicates a slight texture of the α-grains, whereas Fig. 4b clearly reveals a preferential orientation. The preferred orientation can be rationalized by epitaxial solidification and growth upon solidification. As previously described, the irregular orientation is assumed to be caused by an accumulation of small α-grains in the centre of the weld seam. Similar to the findings of Vollmer et al. [28], the fraction of α-phase increases with increasing process energy. This is also substantiated by the intensity loss of the (111)γ diffraction peak in Fig. 4b in comparison to Fig. 4a. The higher mean arc linear energy leads to a higher α-phase fraction, however, γ-phase decoration and precipitation still occurs. Along with the increased mean arc linear energy, the γ-phase fraction increases due to the lower cooling rate and a higher rate of phase transformation (Fig. 4c). Within the welds, no influence of MnS or Al_2S_3 precipitation on formation of the other phases was observed.

Figure 5 shows the HAZ of the square butt welds. While large elongated α-grains (dark) are present in the FZ, in the HAZ an equiaxed microstructure of the α-grains can be observed. Comparing Fig. 5a with Fig. 5f, an increase in γ-phase (bright) fraction is visible. Although grain growth with increasing energy input can be observed in the FZ, this is not evident in the HAZ. The average equivalent grain diameter remains in the range of 110 to 120 μm. In addition, less γ' martensite occurs in the HAZ as needle-like structures inside the α-grains. The high γ-phase fraction supresses the MT so that less γ' martensite forms as previously discussed.

When comparing the relative intensities of the (111)γ diffraction peaks in Fig. 6, the increase in γ-phase fraction with increasing energy input can be clearly seen. The α-grains seem to remain unaffected by the increasing heat input. Due to the high γ-phase fraction, a degradation of the functional properties is to be expected, especially in the HAZ.

In addition to a high (α/γ)-ratio and a minor γ' martensite fraction being present, it is required that the HAZ and FZ of the joined Fe-SMA can transfer the necessary stress required to exploit the MT in damping applications. In order to estimate if the HAZ and FZ could transfer the necessary stress, a hardness measurement was carried out (Fig. 7) and compared with reported hardness values of non-heat–treated and heat–treated material, which eventually showed pseudoelasticity in the aged condition. For this measurement, the specimen with the least γ-phase fraction was chosen (Q = 240 J/mm). As discussed previously, a high γ-phase fraction in the HAZ favours degradation upon cyclic loading and supresses MT.

The hardness of the BM is similar to the value determined by Krooß et al. for an alloy processed using laboratory equipment [27]. In Fig. 7, it can be seen that the hardness slightly decreases during transition from the BM to the HAZ (zone A in Fig. 7). This might be caused by a transformation of the remaining α-phase of the BM. Because of the low temperatures in this distinct region of the HAZ, transformation from α→γ takes place. This brings the hardness to lower values than in the BM. Due to the significant increase in terms of the α-phase fraction from zone A to zone B of the HAZ, hardness then increases steeply. In the FZ, the localized influence of the γ-phase becomes obvious. The hardness value reaches its maximum in the FZ; however, the still relatively high fraction of γ-segregations (cf. Figure 3) leads to a significant scattering of the hardness values across this zone. The average hardness of the FZ complies with the hardness of bamboo-like heat-treated specimens (in solutionized and quenched condition) reported by Krooß et al. [27]. It should be noted that the hardness reported in that paper results from a pure α-matrix, whereas the hardness values of the FZ in Fig. 7 are dominated by the mixture of α-grains and large fractions of γ' martensite and γ-phase. Krooß et al. reported significantly higher values in the as-welded FZ after electron beam welding [27]. The high hardness values seen in that study
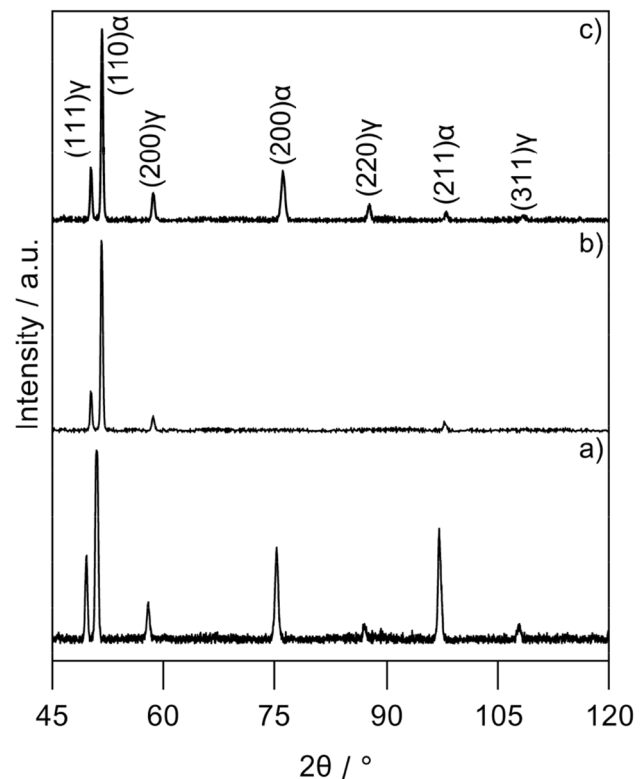

Fig. 4 XRD patterns with subtracted background of the FZ for welds with matching filler material and 70/30 Ar/He; welding parameters are: (a) 120 A, v = 300 mm/min, Q = 240 J/mm, (b) 130 A, v = 300 mm/min, Q = 260 J/mm and (c) 160 A, v = 400 mm/min, Q = 331 J/mm

were attributed to the α-phase microstructure and the potential presence of nanoscale precipitates (β-NiAl-phase), which already could have been formed during cooling upon welding. Such precipitates could have been additionally formed in thepresent work as well. Although the average hardness of the FZ (Fig. 7) indicates that the FZ may be able to transfer the stress necessary for MT, the influence (and the affect) of the present phases still needs to be evaluated in future studies. Furthermore, the minor loss of hardness in the HAZ and adjacent material could lead to premature failure of the weld upon cyclic loading. Especially when heat-treated material, which reaches hardness values similar to the FZ, is joined and cyclically loaded, this area is particularly critical.

3.3 Heat-treated base material

To evaluate the influence of prior heat treatment of the BM, with the aim of large α-grains in the HAZ and FZ and sufficient γ-phase to supress intergranular cracking, an additional experiment was run. Prior to welding the BM was first solution annealed at 1473 K for 15 min, cooled at air and then welded. The heat-treated sheet was joined with a current of 105 A. Figure 8 shows the cross-section of the HAZ of the joined specimen. In this case, neither intergranular cracking nor extensive γ-phase precipitation took place. In the HAZ of the heat-treated specimen an α-grain size in the transverse direction of nearly 1 mm was achieved. At the same time, the major axis of the α-grains in the FZ increased to about 2 mm. Thus, a clear influence of the initial microstructure of the BM on grain morphology and grain growth in the HAZ and FZ becomes apparent. It is assumed that the higher α/γ-ratio of the heat-treated BM favours grain growth by epitaxial growth of the α-phase in the HAZ and at the same time supresses the nucleation of the γ-phase. This enables a significantly improved stress transmission between the BM and the weld zone and, thus, to counteract a failure of the weld seam. In addition, the α-phase content in the HAZ increases the ability to react to external stresses by a MT. The influence of the

Fig. 5 OM of the HAZ of square butt welds with matching filler material and 70/30 Ar/He; welding parameters are: (a) 120 A, v = 300 mm/min, (b) 130 A, v = 300 mm/min, (c) 140 A, v = 300 mm/min, (d) 140 A, v = 400 mm/min, (e) 150 A, v = 400 mm/min and (f) 160 A, v = 400 mm/min; calculated mean arc linear energy is given beneath each individual micrograph

a) Q = 240 J/mm

d) Q = 255 J/mm

b) Q = 260 J/mm

e) Q = 290 J/mm
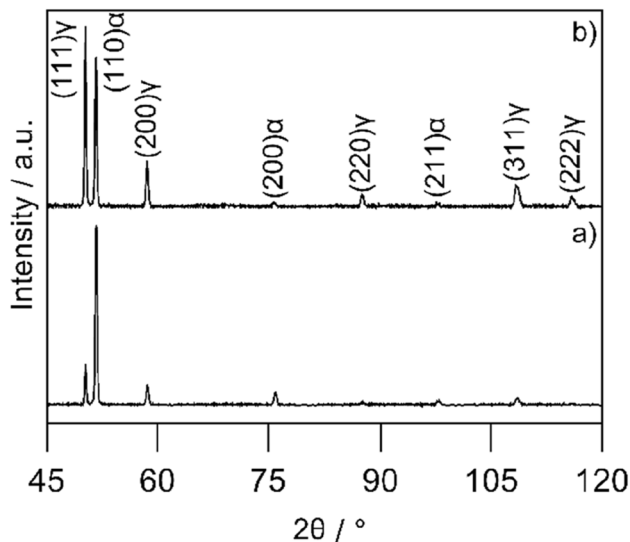
c) 200 µm Q = 285 J/mm

f) 200 µm Q = 331 J/mm
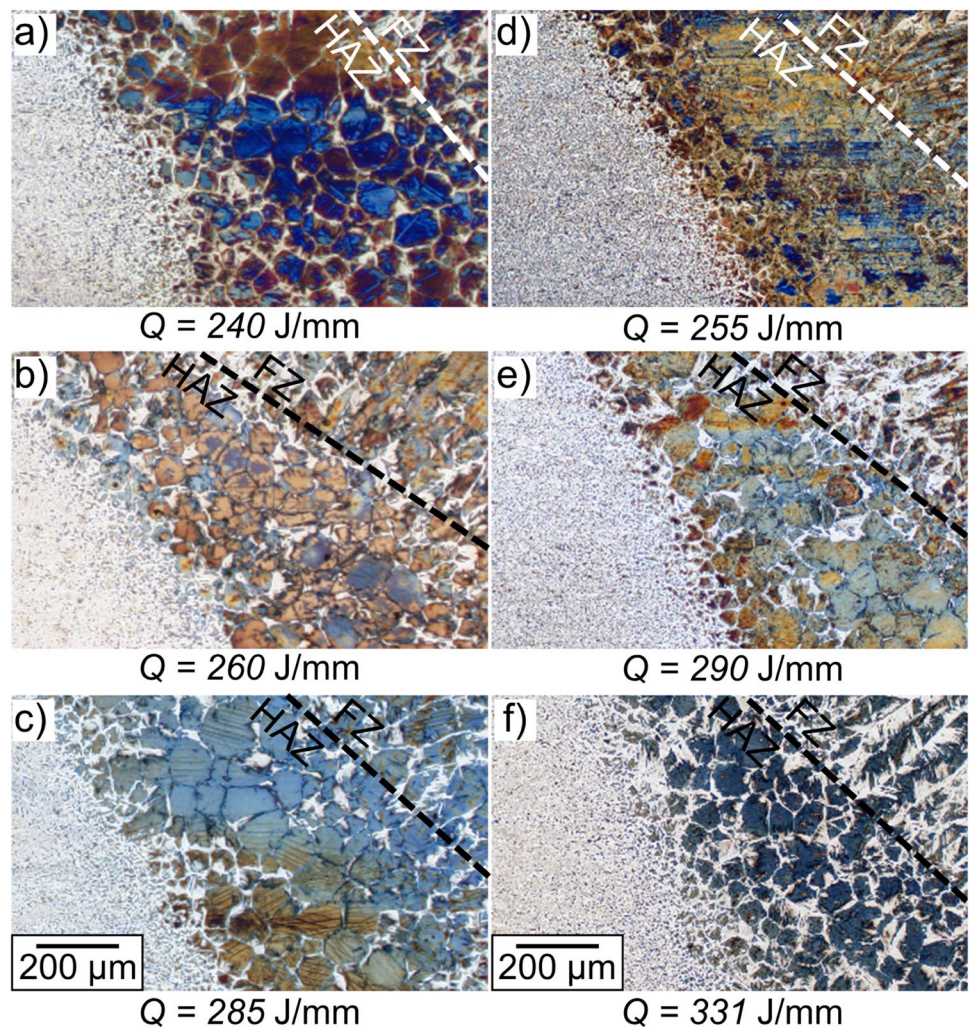
Fig. 6 XRD patterns with subtracted background of the HAZ for the square butt welds with matching filler material and 70/30 Ar/He; welding parameters are: (a) 120 A, v = 300 mm/min, Q = 240 J/mm and (b) 160 A, v = 400 mm/min, Q = 331 J/mm
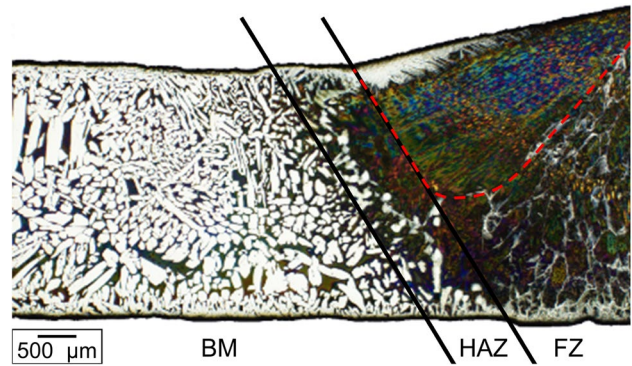

Fig. 8 Cross-section of a specimen heat-treated prior to welding with 105 A and 70/30 Ar/He; the red dashed line indicates a single α-grain in the FZ

microstructure of the BM on the HAZ and FZ on the actual shape memory properties of the as-welded state needs further study, and work is underway to address this issue.

microscopy and X-ray diffraction. The main results can be summarised as follows.

1) Shielding gas composition and mean arc linear energy have a substantial impact on the phases formed in the fusion zone (FZ) and the heat affect zone (HAZ). Lower He content affects the heat input and, thus, leads to less γ-phase precipitation in the α-matrix and along the grain boundaries. Given the lower heat input during welding, intercrystalline cracking results. By varying the mean arc linear energy, the γ-phase fraction in the FZ can be controlled. Eventually, this effect can be exploited to suppress intergranular cracking.

2) Elongated α-grains with a preferential orientation can be observed in the FZ. With increasing mean arc linear energy grain growth occurs, so that the length of the major axis of the elongated grains also increases. No influence of MnS and Al_2S_3 precipitates on the formation of the other phases in the FZ as well as in the HAZ can be observed.

3) In the HAZ, an equiaxed microstructure with a high γ-phase fraction evolves. This causes a reduction of the hardness in the HAZ in comparison to the FZ. In addition, a phase transformation from α-phase to γ-phase takes place in distinct regions with relatively low temperatures of the HAZ. Because of this phase transformation, the hardness locally drops below the value of the polycrystalline α + γ base material. This local softening is critical with respect to cyclic loading.

4) Grain morphology and grain growth in the HAZ and FZ are affected by the microstructure and the α/γ-ratio of the BM. Welding solution annealed (1473 K for 15 min) BM leads to large α-grains with a major axis length up to 2 mm. The (α/γ)-ratio in the HAZ and FZ is increased compared to the square butt welds without prior heat-treatment.

4 Conclusions

The welding characteristics and microstructure of an industrially processed $FeMn_{34}Al_{15}Ni_{7.5}$ (at.%) shape memory alloy joined by tungsten inert gas welding were investigated using optical microscopy, scanning electron

Fig. 7 Hardness measurement of the as-welded state for a specimen welded with 120 A, v = 300 mm/min, and Q = 240 J/mm; indicating α → γ transformation in zone A and enhanced α-grain growth in zone B; see text for details

Declarations

Competing interests The authors declare no competing interests.

References

1. Omori T, Ando K, Okano M, Xu X, Tanaka Y, Ohnuma I, Kainuma R, Ishida K (2011) Superelastic effect in polycrystalline ferrous alloys. Science 333:68–71. https://doi.org/10.1126/science.1202232

2. Kajiwara S (1999) Characteristic feature of shape memory effect and related transformation behaviour in Fe-based alloys. Matr Sci Eng A 273:67–88. https://doi.org/10.1016/S0921-5093(99)00290-7

3. Maki T, Furutan S, Tamura I (1989) Shape memory effect related to thin plate martensite with large thermal hysteresis in ausaged Fe-Ni-Co-Ti alloy. ISIJ Int 29:438–445. https://doi.org/10.2355/isijinternational.29.438

4. Sato A, Chishima E, Soma K, Mori T (1982) Shape memory effect in $\gamma \rightleftarrows \varepsilon$ transformation in Fe-30Mn-1Si alloy single crystals. Acta Metall 30:1177–1183. https://doi.org/10.1016/0001-6160(82)90011-6

5. Wayman CM (1971) On memory effects related to martensitic transformation and observations in β-brass and Fe_3Pt. Scr Metall 5:489–492. https://doi.org/10.1016/0036-9748(71)90097-4

6. Chumlyakov YI, Kireeva IV, Poklonov VV, Pobedennaya ZV, Karaman I (2014) The shape-memory effect and superelasticity in single-crystal ferromagnetic alloy FeNiCoAlTi. Tech Phy Lett 40:747–750. https://doi.org/10.1134/S1063785014090053

7. Omori T, Abe S, Tanaka Y, Lee DY, Ishida K, Kainuma R (2013) Thermoelastic martensitic transformation and superelasticity in Fe-Ni-Co-Al-Nb-B polycrystalline alloy. Scr Mater 69:812–812. https://doi.org/10.1016/j.scriptamat.2013.09.006

8. Tanaka Y, Himuro Y, Kainuma R, Sutou Y, Omori T, Ishida K (2010) Ferrous polycrystalline shape-memory alloy showing huge superelasticity. Science 327:1488–1490. https://doi.org/10.1126/science.1183169

9. Vollmer M, Arold T, Kriegel MJ, Klemm V, Degener S, Freudenberger J, Niendorf T (2019) Promoting abnormal grain growth in Fe-based shape memory alloys through compositional adjustments. Nat Commun. https://doi.org/10.1038/s41467-019-10308-8

10. Vollmer M, Krooß P, Karaman I, Niendorf T (2017) On the effect of titanium on quenching sensitivity and pseudoelastic response in Fe-Mn-Al-Ni base shape memory alloy. Scr Mater 126:20–23. https://doi.org/10.1016/j.scriptamat.2016.08.002

11. Omori T, Kusama T, Kawata S, Ohnuma I, Sutou Y, Araki Y, Ishida K, Kainuma R (2013) Abnormal grain growth induced by cyclic heat treatment. Science 341:1500–1502. https://doi.org/10.1126/science.1238017

12. Tseng LW, Ma J, Vollmer M, Krooß P, Niendorf T, Karaman I (2016) Effect of grain size on the superelastic response if a FeMnAlNi polycrystalline shape memory alloy. Scr Mater 125:68–72. https://doi.org/10.1016/j.scriptamat.2016.07.036

13. Tseng LW, Ma J, Wang SJ, Karaman I, Kaya M, Luo ZP, Chumlyakov YI (2015) Superelastic response of a single crystalline FeMnAlNi shape memory alloy under tension and compression. Acta Mater 89:374–383. https://doi.org/10.1016/j.actamat.2015.01.009

14. Tseng LW, Ma J, Chumlyakov YI, Karaman I (2019) Orientation dependence of superelasticity in FeMnAlNi single crystals under compression. Scr Mater 166:48–52. https://doi.org/10.1016/j.scriptamat.2019.02.034

15. Tseng LW, Mia J, Wang SJ, Karaman I, Chumlyakov YI (2016) Effects of crystallographic orientation on the superelastic response of FeMnAlNi single crystals. Scr Mater 116:147–151. https://doi.org/10.1016/j.scriptamat.2016.01.032

16. Tseng LW, Ma J, Hornbuckle BC, Karaman I, Thompson GB, Luo ZP, Chumlyakov YI (2015) The effect of precipitates on the superelastic response of [100] oriented FeMnAlNi single crystals under compression. Acta Mater 97:234–244. https://doi.org/10.1016/j.actamat.2015.06.061

17. Ueland SM, Schuh CA (2013) Grain boundary and triple junction constraints during martensitic transformation in shape memory alloys. J Appl Phys. https://doi.org/10.1063/1.4817170

18. Ueland SM, Schuh CA (2012) Superelasticity and fatigue in oligocrystalline shape memory alloy microwire. Acta Mater 60:282–292. https://doi.org/10.1016/j.actamat.2011.09.054

19. Ueland SM, Chen Y, Schuh CA (2012) Oligocrystalline shape memory alloys. Adv Funct Mater 22:2094–2099. https://doi.org/10.1002/adfm.201103019

20. Omori T, Okano M, Kainuma R (2013) Effect of grain size on superelasticity in Fe-Mn-Al-Ni shape memory alloy wire. APL Mater. https://doi.org/10.1063/1.4820429

21. Omori T, Iwaizako H, Kainuma R (2016) Abnormal grain growth induced by cyclic heat treatment in Fe-Mn-Al-Ni superelastic alloy. Mater Des 101:263–269. https://doi.org/10.1016/j.matdes.2016.04.011

22. Vollmer M, Segel C, Krooß P, Günther J, Tseng LW, Karman I, Weidner A, Biermann H, Niendorf T (2015) On the effect of gamma phase formation on the pseudoelastic performance of polycrystalline Fe-Mn-Al-Ni shape memory alloy. Scr Mater 108:23–26. https://doi.org/10.1016/j.scriptamat.2015.06.013

23. Li S, Hedayati Dezfuli F, Wang J, Alam MS (2020) Performance-based seismic loss assessment of isolated simply-supported highway bridges retrofitted with different shape memory alloy cable restrainers in a life-cycle context. J Intell Mater Syst Struct. https://doi.org/10.1177/1045389X20906018

24. Abbass A, Attarneja R, Ghassemieh M (2020) Seismic assessment of RC bridge columns retrofitted with near-surface mounted

shape memory alloy technique. Materials. https://doi.org/10.3390/ma13071701

25. Lin HC, Lin KM, Chuang YC, Chou TS (2000) The welding characteristics of Fe-30Mn-6Si and Fe-30Mn-5Cr shape memory alloys. J Alloys Compd 306:186–192. https://doi.org/10.1016/S0925-8388(00)00762-3

26. Zhou CY, Lin CX, Liu LL (2010) Study on YAG laser welding process of Fe-Mn-Si shape memory alloy. Appl Mech Mater 37–38:1364–1367. https://doi.org/10.4028/www.scientific.net/AMM.37-38.1364

27. Krooß P, Günther J, Halbauer L, Vollmer M, Buchwalder A, Zenker R, Biermann H, Niendorf T (2017) Electron beam welding of Fe-Mn-Al-Ni shape memory alloy: microstructure evolution and shape memory response. Funct Mater Lett. https://doi.org/10.1142/S1793604717500436

28. Vollmer M, Baunack D, Janoschka D, Niendorf T (2020) Induction butt welding followed by abnormal grain growth: a promising route for joining of Fe-Mn-Al-Ni tubes. Shap Mem Superelasticity 6:131–138. https://doi.org/10.1007/s40830-019-00261-2

29. Murphy AB, Tanaka M, Tashiro S, Sato T, Lowke JJ (2009) A computational investigation of the effectiveness of different shielding gas mixtures for arc welding. J Phys D Appl Phys 42:11. https://doi.org/10.1088/0022-3727/42/11/115205

30. Ojha A, Sehitoglu H (2016) Transformation stress modeling in new Fe-Mn-Al-Ni shape memory alloy. Int J Plast 86:93–111. https://doi.org/10.1016/j.ijplas.2016.08.003